Strong electron-phonon coupling superconductivity in compressed α-MoB_2 induced by double Van Hove singularities

Xiaohan Liu,[1] Xiaowei Huang,[1,2] Peng Song,[3,1] Chongze Wang,[4] Liying Zhang,[1] Peng Lv,[1] Liangliang Liu,[1,2,*] Weifeng Zhang,[2] Jun-Hyung Cho,[4] and Yu Jia[1,2,5,†]

[1]*Key Laboratory for Special Functional Materials of Ministry of Education, and School of Materials Science and Engineering, Henan University, Kaifeng, 475004, China*

[2]*Joint Center for Theoretical Physics, Henan University, Kaifeng 475004, China*

[3]*The Grainger College of Engineering, University of Illinois at Urbana-Champaign, Lincoln Hall, 702 S Wright St, Urbana, Illinois 61801, USA*

[4]*Department of Physics, Research Institute for Natural Science, Hanyang University, 222 Wangsimni-ro, Seongdong-Ku, Seoul 04763, Korea*

[5]*International Laboratory for Quantum Functional Materials of Henan, Zhengzhou University, Zhengzhou 450001, China*

(Received 20 May 2022; revised 6 August 2022; accepted 8 August 2022; published 17 August 2022)

A recent experiment of MgB_2-type structure α-MoB_2 has realized ~32 K superconductivity (SC) at 90 GPa, exhibiting the highest superconducting transition temperature (T_c) among transition-metal diborides. Although the SC was characterized by the electron-phonon coupling (EPC), the microscopic mechanism of how the large EPC constant and high T_c are attained is unclear. Here, based on first-principles calculations, we found that in contrast to MgB_2, B atoms contribute most to electronic states near Fermi level (E_F), Mo d_{z^2} orbital is more dominant component in MoB_2 and provides two impressive peaks in density of states near E_F associated with emergent double Van Hove singularities (VHS). The EPC analysis reveals that the electronic sates around double VHS could strongly interact with the softened acoustic modes of Mo out-of-plane vibration, giving rise to a large single gap with the T_c up to ~37 K, which distinctly differs from the superconducting feature of MgB_2. Furthermore, by electron doping into MoB_2, the VHS is tuned to be aligned with the E_F and T_c can be increased to ~43 K. Our findings not only elucidate the microscopic mechanism of observed high T_c in MoB_2, but also demonstrate that MoB_2 provides an ideal platform to explore the role of the VHS in emergent strong EPC SC.

DOI: 10.1103/PhysRevB.106.064507

I. INTRODUCTION

Ever since the discovery of superconductivity (SC) in metal mercury at 4.2 K a century ago [1], realization of higher superconducting transition temperature (T_c) has been one of long-sought goals in condensed matter physics and material science [2,3]. In 2001, metal diboride MgB_2 was reported to obtain phonon-mediated SC with the T_c up to ~39 K [4], approaching the McMillan limit, and subsequently, a great amount of effort has been paid for designing and searching for new boride superconductors theoretically and experimentally. Investigation of isostructural metal diborides MB_2 (M = Al, Sc, Zr, Ta, and Y [5–8]) has shown that only few of them seem to be superconducting, and MgB_2-type layered boron carbides including Li_2B_3C, $Li_4B_5C_3$, and $Li_{2x}BC_3$ are predicted to have higher T_c of 40 ~55 K [9,10]. However, we are not aware of experimental progress on these predictions. Beyond the framework of traditional Bardeen-Cooper-Schrieffer (BCS) theory, cuprate and pnictide superconductors greatly enrich the families of superconducting materials and their T_cs can reach above 100 K, which opens the new field of SC research [11,12]. While to date the superconducting mechanism of cuprate and pnictide remains controversial [13,14], and it in turn hinders further increase of the T_c.

Pressure, a fundamental thermodynamic variable, was demonstrated to play an important role in the superconducting research, and provides an effective route to enhance SC by inducing phase transition or altering interatomic interactions [15,16]. It has continued to be used to set new record high T_c in cuprate, pnictide, and hydride superconductors. For example, through the heroic efforts of numerous scientists, under 31 GPa the T_c has been climbed above 164 K in the $HgBa_2Ca_2Cu_3O_{8+\delta}$ cuprate [17]. For high-pressure hydride superconductors, a unique compound H_3S with T_c = 191 ~ 204 K had been predicted and then obtained under 150 GPa experimentally [18,19], opening a new era of superconducting study. In the following, theoretically predicted LaH_{10} was synthesized with the T_c of 250 ~ 260 K at a pressure of 170 ~ 180 GPa [20–23]. A higher T_c of 288 K was reported in the carbonaceous sulfur hydride at ~267 GPa [24], achieving coveted room-temperature SC. These achievements undoubtedly point out that high pressure is a powerful tool to tune properties of materials and then realize novel high-T_c superconductors.

Recently, Pei *et al.* carried out a high-pressure study on the transition-metal diboride MoB_2 and surprisingly they discovered that the application of high pressure drives the β phase transition into α phase (MgB_2-type structure) associated with

*Corresponding author: liull@henu.edu.cn
†Corresponding author: jiayu@zzu.edu.cn

T_c as high as ∼32 K at 90 GPa [25], which exhibits the highest T_c among all transition-metal diborides. Although this observed SC in compressed α-MoB_2 has been described by the BCS theory [25,26], a microscopic understanding of what makes α-MoB_2 so different from other boride superconductors and why α-MoB_2 features such a strong electron-phonon coupling (EPC) is missing. It is therefore necessary to investigate the salient electronic, bonding, and phononic properties of α-MoB_2 from which large EPC is derived.

In this paper, we carried out first-principles calculation combined with anisotropic Migdal-Eliashberg (M-E) theory [27,28] to study superconducting properties of compressed α-MoB_2. We found Mo d orbitals contribute most to the electronic states near Fermi level (E_F), and especially d_{z^2} orbital provides two impressive peaks associated with emergent double Van Hove singularities (VHS). The further EPC analysis demonstrates that the electronic states near double VHS could effectively interact with Mo out-of-plane stretching modes, giving rise to a large superconducting gap and thus to obtain high T_c of 33.1 ∼ 37 K. This superconducting feature is essentially different from MgB_2 case that B σ states induce 39 K SC by coupling with the high-frequency in-plane vibrations of B atoms [29]. Furthermore, we propose that with electron doping in α-MoB_2, the VHS was shifted down to be aligned with the E_F to enhance the EPC, thereby resulting in the increase of the T_c to ∼43 K. Our findings shed light on the importance of the VHS in obtaining strong EPC SC and reveal the microscopic mechanism of observed high-T_c SC in compressed α-MoB_2.

II. CALCULATIONAL METHODS

Our DFT calculations were performed using the Vienna *ab initio* simulation package (VASP) with the projector-augmented wave (PAW) method [30–32]. For the exchange-correlation energy, we employed the generalized-gradient approximation functional of Perdew-Burke-Ernzerhof (PBE) [33]. The **k**-space integration was done with $21 \times 21 \times 21$ k-point grid for structure optimization, and a plane-wave basis was taken with a kinetic energy cutoff of 500 eV. All atoms were allowed to relax along the calculated forces until all the residual force components were less than 0.005 eV/Å. The subsequent lattice dynamics and EPC calculations were carried out by using the QUANTUM ESPRESSO (QE) package [34] with the optimized norm-conserving Vanderbilt (ONCV) pseudopotentials [35] and a plane-wave cutoff of 80 Ry. Here, we used $5 \times 5 \times 3$ q-point grid for the computation of MoB_2 phonon. The anisotropic M-E equations with a typical Coulomb pseudopotential parameter of $\mu = 0.13$ and 0.15 [20,25,36] are employed to calculate the superconducting gap and estimate the T_c of the α-MoB_2 as implemented in electron-phonon Wannier (EPW) code [37], and the interpolated k-point grid of $50 \times 50 \times 40$ and q-point grid of $25 \times 25 \times 20$ are used in the superconducting calculations.

III. RESULTS

We begin by optimizing the bulk α-MoB_2 [see Figs. 1(a) and 1(b)] using the PBE calculations under 90 GPa, and obtained lattice parameters are $a = b = 2.861$ Å and $c = 3.082$ Å, respectively, in good agreement with the previous data of $a = b = 2.884$ Å and $c = 3.017$ Å [26]. In the bulk structure, Mo atoms are intercalated between two B-B layers and occupy at the honeycomb center. The calculated total charge density of MoB_2 is displayed in Fig. 1(c). It is seen that B atoms are covalently bonded to each other, and the charge density at their midpoints are 1.0 e/Å^3, larger than the 0.8 e/Å^3 of B-B bonds in MgB_2 [see Fig. 1(d)], indicating that the B-B bonds in MoB_2 exhibit stronger covalent bonding characters. Interestingly, Mo atoms not only donate their part of valance electrons (Bader analysis [38]: 0.92 e$^-$) to B atoms, but also are covalently connected to B atoms, and calculated electrical charges at the midpoint of Mo-B bond are ∼0.6 e/Å^3, demonstrating a mixed ionic-covalent bond between Mo and B atoms. Additionally, subsequent calculation of partial charge density shows there also exist weak covalent bonds between two neighboring Mo atoms, as shown in Fig. 2(d). This bonding behavior is entirely different from MgB_2, where Mg atoms just donate their valence electrons to the B-B layer and have pure ionic bonds with B atoms [see Fig. 1(d)].

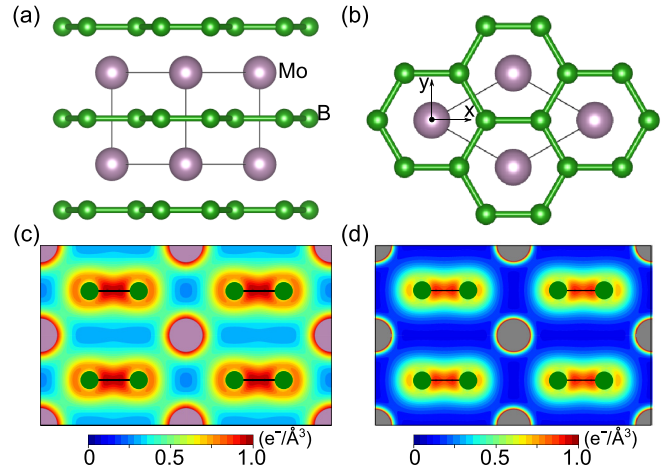

FIG. 1. (a) Side view and (b) top view of α-MoB_2 structural configuration under 90 GPa. (c) and (d) show total charge density of MoB_2 under 90 GPa and MgB_2, respectively, plotted on the $(1\bar{1}0)$ surface of the 2×2 supercell. The charge density contour maps are drawn in the $(1\bar{1}0)$ plane with a contour spacing of 0.05 e/Å^3.

Since MoB_2 has the P6/mmm space group, the crystal field analysis demonstrates that Mo 4d orbitals (Mo site: D_{6h} point group) would be split into a singlet a_{1g} (d_{z^2}) and two doublets e_{1g} (d_{xz} and d_{yz}) and e_{2g} (d_{xy} and $d_{x^2-y^2}$), and B p orbitals (B site: D_{3h} point symmetry) split into a singlet a_2'' (p_z) and a doublet e' (p_x and p_y). Figure 2 shows the calculated projected band structure (Pband), partial density of states (PDOS), and partial charge density, respectively. In Fig. 2(a), the band structure exhibits that there are four bands (denoted as $n = 1$, 2, 3, and 4) across the E_F, together with projection of their electronic states onto the Mo d_{z^2} and B p_z orbitals. Compared to other orbitals, Mo d_{z^2} is more dominant component of the electronic states located near E_F (see Fig. S1 in Supplemental Material [39]), and has some weak hybridization with minority state of B p_z orbital along the k-path L-V-N-K of Brillouin

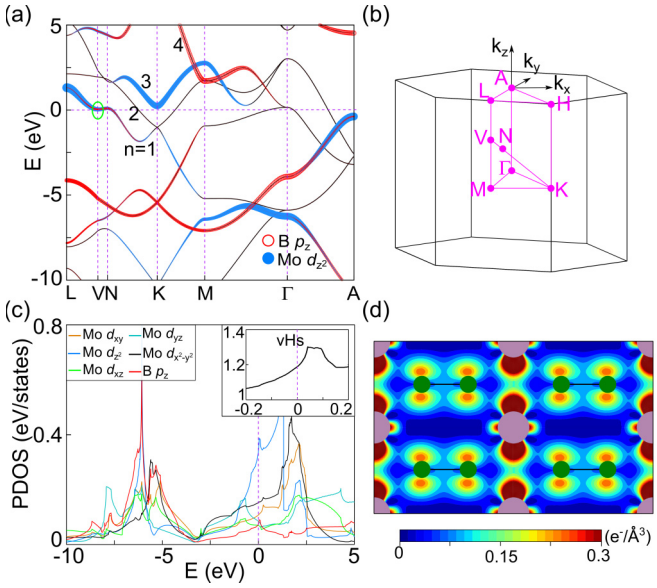

FIG. 2. (a) Calculated band structure and (c) partial DOS of α-MoB_2. In (a), the bands projected onto the Mo d_{z^2} and B p_z orbitals are displayed with circles whose radii are proportional to the weights of the corresponding orbitals. A closeup of the total DOS around the VHS is given in the inset of (c). The energy zero represents E_F. (b) Brillouin zone of primitive cell α-MoB_2. (d) Calculated partial charge density of VHS at the k-point V [green ellipse in (a)], plotted on the $(1\bar{1}0)$ surface of the 2×2 supercell.

zone in Fig. 2(b). It is noteworthy that the energetic dispersion of band $n = 1$ shows the presence of a holelike band along the path L-V-N while electronlike band along the path V-N-K. These two holelike and electronlike bands fortunately meet at k points V and N, giving rise to two Van Hove singularities associated with larger localized electronic states near E_F [see Fig. 2(c)]. The charge character of the VHS at the k point V [see Fig. 2(d)] shows that due to the hybridization of the d_{z^2} orbitals, two neighboring Mo atoms are covalently connected with weak σ bond, having a saddle point of charge density at its middle, which is similar to the C-C σ bond in diamond [40]. This result reveals that the emergence of the VHS is closely related to the formation of the Mo-Mo σ bonds.

To measure the strength of the VHS, using the local principal-axis coordinates, we obtain the effective masses m_1, m_2, and m_3 of the holelike band as $-2.389\ m_e$, $0.568\ m_e$, and $0.381\ m_e$ (thermal mass $m_{th} \equiv |\ m_1 m_2 m_3\ |^{1/3} = 0.803\ m_e$), and we obtain electronlike band as $-0.259\ m_e$, $-0.712\ m_e$, and $0.341\ m_e$ ($m_{th} = 0.397\ m_e$). Note that the larger the thermal mass, the larger the strength, and the flatter is the hole or electronlike band. Figure 2(c) displays a closeup of the total DOS around the VHS, which represents the presence of two Van Hove singularities separated by $\Delta E_{VHS} = 40$ meV. Such double VHS also appeared in compressed hydride superconductors LaH_{10} and H_3S, and was demonstrated to play an important role in enhancing the EPC [41,42]. Additionally, we further calculate electronic structure of α-MoB_2 under 60 GPa and 120 GPa, compared with that at 90 GPa (see Fig. S2 in Supplemental Material [39]), and find that the double VHS remain very stable to be insensitive to the change

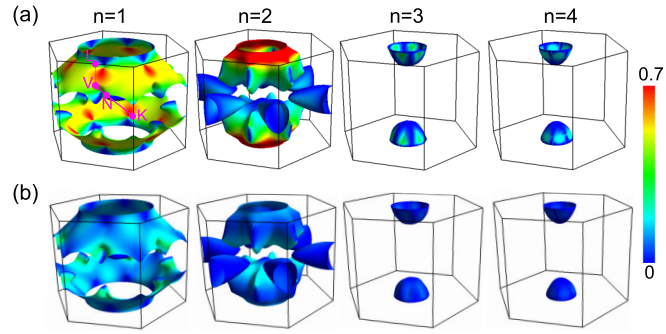

FIG. 3. The corresponding FS sheets for the four bands of $n = 1$, 2, 3, and 4. The electronic state at each FS sheet is respectively projected onto (a) Mo d_{z^2} and (b) B p_z orbitals using the color scale in the range [0, 0.7].

of pressure. GGA + U method is also used to examine the correlation effect, and we found it does not influence the electronic structures of MoB_2 (see the Fig. S3 in Supplemental Material [39]). Figures 3(a) and 3(b) display the four FS sheets with the projection of Mo d_{z^2} and B p_z orbitals, respectively. It is seen that the first and second FS sheets with the complex shape spread over the large regions in the Brillouin zone, and Mo dz^2 and B p_z orbitals are mainly distributed on these two FS sheets. We note that, consistent with band calculation, the electronic states surrounding the k points V and N on the first FS sheet, e.g., double Van Hove singularities, are mostly composed of the Mo dz^2 orbital, and B p_z orbital has a small contribution. The third and fourth FS sheets are topologically similar with bowl shapes surrounding the k point Z, which mainly come from the contribution of B p_x/p_y and Mo d_{zx}/d_{zy} (see Fig. S4 in Supplemental Material [39]). Such anisotropic orbital characters on the FS are naturally expected to invoke different couplings between the various bands, leading to the emergence of anisotropic EPC strength and superconducting gaps on the FS.

Having investigated the bonding nature and electronic structure of α-MoB_2, we go on to examine its phonon properties and EPC within density functional perturbation theory (DFPT) [43]. The resulting phonon band structure indicates that this is a phonon gap of ~20 meV between high-frequency optical branches and low-frequency acoustic branches. From the atom-mode projected phonon spectrums in Fig. 4(a), it is revealed that the optical branches mostly arise from the in-plane and out-of-plane vibrations of B atoms, and exhibit relatively flat dispersion compared to MgB_2 (see Fig. S5 in Supplemental Material [39]). Meanwhile, because the dominant component of B electronic states is far away from the E_F and strong B-B bonds result in the stiffness of B vibrations, these phononic modes have very weak EPC [see Fig. 4(b)]. Interestingly, we note that along the q path A-L-H, the acoustic modes contributed by the Mo out-of-plane vibrations suffer a sharp softening, and make great contributions to the EPC. Especially, Mode I drives the strongest EPC by stretching and compressing the weak Mo-Mo σ bonds [see Figs. 4(b)–4(c)], which is also manifested by the fact that double-VHS band (e.g., Mo σ-bonding states) obviously moves up as the atomic displacements of Mode I according to the unfolding band dispersion of primitive cell in Fig. 4(d). The underlying concept

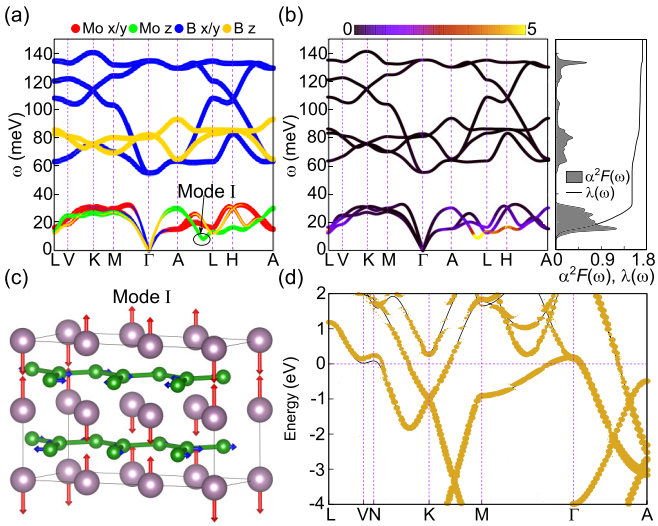

FIG. 4. (a) Phonon spectrum projected on atomic in-plane (x/y) and out-of-plane (z) vibrations. (b) Phonon spectrum with projection of EPC strength λ_{qv} using the color scale in the range [0, 5], and the isotropic Eliashberg function $\alpha^2F(\omega)$ with integrated EPC constant $\lambda(\omega)$. (c) Atomic displacements of the Mode I, labeled as indicated in (a). Here, since Mode I corresponds to the q-point coordinate of about number $(\frac{1}{3}, 0, \frac{1}{2})$, a $3 \times 1 \times 2$ supercell was employed to fold this q point into the Brillouin zone center. The arrows on Mo/B atoms indicate vibrational directions and magnitudes (Mo: 0.04 Å, B: 0.012 Å). (d) The unfolding band structure (yellow points) with the atomic displacements of Mode I, plotted along the same k path of equilibrium structure in the primitive cell (bottom black lines) to facilitate comparison.

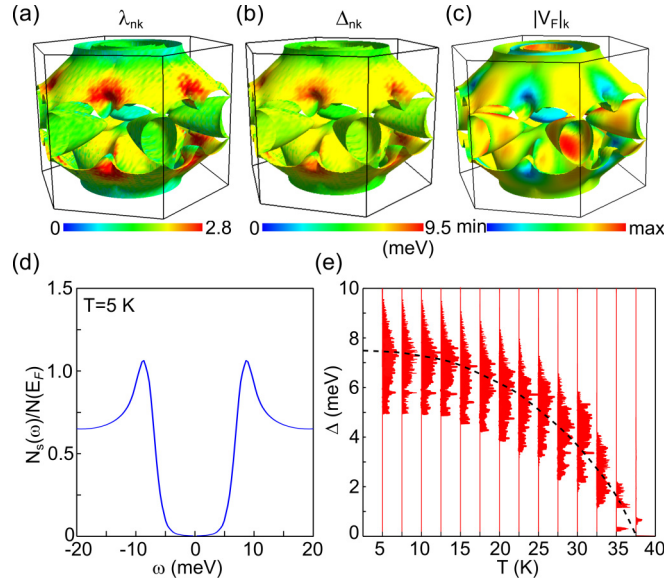

FIG. 5. Calculated k-resolved (a) EPC constant λ_{nk}, (b) superconducting gap Δ_{nk} at 5 K, and (c) Fermi velocity $|V_F|_k$ projected on the four FS sheets represented by color scale. (d) The normalized quasiparticle DOSs at 5 K. (e) Energy distribution of the anisotropic superconducting gap Δ versus T for MoB_2. The black dash represents the average value of the superconducting gap.

is that a phonon that is strongly coupled to FS states will produce a large energetic shift in k for states near the E_F [44].

To quantitatively evaluate the EPC strength of the MoB_2, we further calculated the isotropic Eliashberg spectral function $\alpha^2F(\omega)$ through the Wannier interpolation approach based on the equation [45]:

$$\lambda(\omega) = 2\int_0^{\omega} d\omega' \alpha^2F(\omega')/\omega'. \quad (1)$$

The obtained total λ is 1.71. From the Fig. 4(b), it is revealed that the acoustic phonon modes mainly contribute to the Eliashberg spectral function $\alpha^2F(\omega)$, and the integral EPC constant $\lambda(\omega)$ increases sharply as the ω increases at the region of acoustic branches, occupying 80% of total λ. It demonstrates that acoustic phonon modes play a major role in strong EPC for MoB_2.

Considering the anisotropic distribution of atomic orbitals on the FS, we here use the anisotropic M-E equations to clearly reveal the **k**-resolved EPC parameter λ_{nk} and superconducting gap Δ_{nk} for the electronic states (**n**, **k**), as employed in MgB_2 superconducting analysis [29]. The **n** represents the band index and all available electron-phonon scattering processes connecting **k** and other **k** points on the FS sheets are included. The distribution of the λ_{nk} and Δ_{nk} on the FS are displayed in Figs. 5(a) and 5(b), respectively. It is seen that the λ_{nk} strength on the FS exhibits significant anisotropy, and the largest λ_{nk} value is caused by the electronic states around the k points V and N, which represent that the localized states near the VHS give rise to the strong EPC. It is well reflected by the small Fermi velocity near the VHS [see Fig. 5(c)]. In general, a small Fermi velocity is favorable for strong EPC [46]. For the calculated k-resolved superconducting gap Δ_{nk}, it is noticeable that the Δ_{nk} values change on each FS sheet without any nodes, indicating the s-wave SC. Meanwhile, we note that the λ_{nk} and Δ_{nk} are correlated with each other, i.e., the larger λ_{nk} strength, the higher Δ_{nk} value. Accordingly, the electronic states near the VHS also give rise to the largest superconducting gap Δ_{nk} of ~9.5 meV, as shown in Fig. 5(b).

We then calculated normalized quasiparticle DOSs in the superconducting state of MoB_2 according to the $\frac{N_S(\omega)}{N_F} = \mathrm{Re}[\frac{\omega}{\sqrt{\omega^2-\Delta^2(\omega)}}]$ [47], which can be used to compare with the experimental tunneling conductance directly. It is seen that there is only a pair of peaks [see Fig. 5(d)], corresponding to a single superconducting gap. As the temperature T increases, the energy gap Δ gradually decreases to zero at ~37 K [see Fig. 5(e)], indicating $T_c = \sim 37$ K. Additionally, we also use the $\mu^* = 0.15$ to calculate the T_c, and the value is ~33.1 K. Therefore, the obtained T_c is located between 33.1 K and 37 K with $\mu^* = 0.13$–0.15, close to the experimental result of the $T_c = \sim 32$ K [25]. Collecting the calculated the electronic and phononic results of α-MoB_2, it clearly reveals that the electronic states near the VHS, e.g., Mo d_{z^2} orbital driven σ-bonding states, are strongly coupled with Mo out-of-plane stretching modes, resulting in a large superconducting gap and thus high T_c. This result indicates that although α-MoB_2 has the same crystal configuration with MgB_2, their electronic structures and superconducting feature are essentially different. In MgB_2, the coexistence of the in-plane σ $(s + p_{x,y})$-bonding states and out-of-plane π

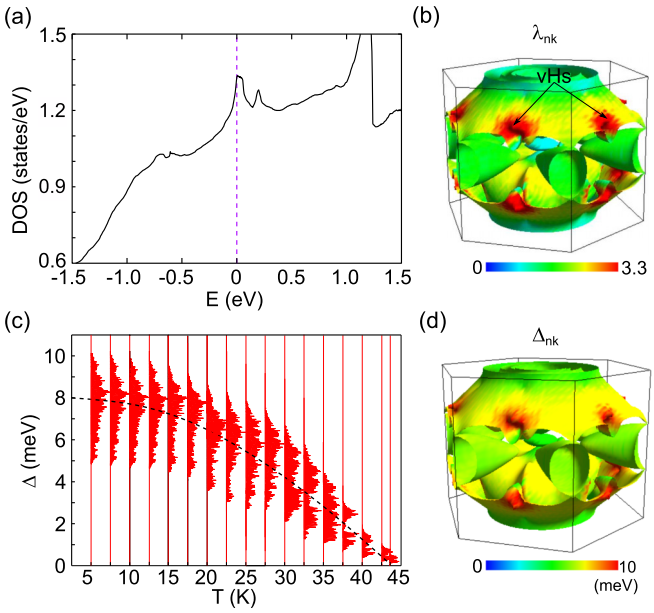

FIG. 6. (a) Total DOS of electron-doping MoB_2 with E_F shifted by 0.04 eV. It is seen that the E_F is crossing the VHS at the kpoint V. (b) Calculated **k**-resolved EPC constant λ_{nk}. (c) Energy distribution of the anisotropic superconducting gap Δ versus T. The black dash represents the average value of the gap Δ. (d) Superconducting gap Δ_{nk} projected on the Fermi sheets, computed at 5 K.

(p_z)-bonding states on the FS gives rise to a separate two-gap nature with the stronger σ gap Δ_σ and the weak π gap Δ_π by coupling with high-frequency in-plane and out-of-plane B vibrations [29,48], respectively. The different bonding, phonon, and superconducting nature in the α-MoB_2 suggest the possibility for exploring new phonon-mediated high-T_c superconductors among transition-metal borides.

Since the energy level of the VHS at the k point V is only 0.04 eV higher than the E_F, this VHS is enabled to shift down toward the E_F with an electron doping of about 0.1 electrons per unit [see Fig. 6(a)]. In order to examine how the VHS influences SC, we use the anisotropic M-E equations to estimate the variations of λ and T_c. We found that with the E_F across the VHS, phonon band dispersion changes a little (see Fig. S6 in Supplemental Material [39]), while, the electronic states at the E_F exhibit more localized dispersion, which results in the enhancement of the EPC strength λ_{nk} on the FS, and Fig. 6(b) shows the largest value near the VHS is 0.5 larger than that of the intrinsic MoB_2. As a result, obtained the largest superconducting gap Δ_{nk} is also increased by $\sim$ 0.5 meV, and the T_c is estimated up to $\sim$43 K, as shown in Figs. 6(c) and 6(d). From the view of the realistic system, this enhanced T_c may be able to be realized in the Re-doped MoB_2 based on the electronic structure calculations, since the Re doping can bring the E_F across the VHS, as shown in the Fig. S7 of Supplemental Material [39], and the further research of EPC and T_c will be a subject in future work. In a word, the present result undoubtedly demonstrates that the VHS plays an essential role in the emergence of strong EPC SC in α-MoB_2.

IV. SUMMARY

In this work, employing first-principles calculation combined with anisotropic Migdal-Eliashberg theory, we have studied the electronic, bonding, and phononic properties of the α-MoB_2. Our study reveals that the emergence of double VHS, which is mainly composed of Mo d_{z^2} orbital, leads to two huge peaks in the density of states near the E_F, and the EPC analysis demonstrates that these localized electronic sates near the VHS are responsible for the 37 K SC by coupling with Mo out-of-plane vibrations. Furthermore, we found that by electron doping in α-MoB_2, the E_F was tuned to cross the VHS associated with T_c increasing to 43 K. These results reflect that the Van Hove singularity plays an essential role in the emergence of strong EPC SC in α-MoB_2. Additionally, we note that there is no Van Hove singularity appearing in the β-MoB_2 (see Fig. S8 in Supplemental Material [39]), which may explain why β-MoB_2 has weak EPC and low T_c of $\sim$5 K [25]. Our present findings not only shed light on the microscopic mechanism of the observed high-T_c SC in compressed α-MoB_2, but also will stimulate further research to explore other high-T_c superconductors among transition-metal diborides.

ACKNOWLEDGMENTS

This work was supported by the National Natural Science Foundation of China (Grants No. 12104129, 12074099 and 11774078), and China Postdoctoral Science Foundation (Grants No. 2020M672201). The superconducting calculations were carried out in National Supercomputing Center in Zhengzhou.

X.H. and X.W. contributed equally to this work.

[1] H. K. Onnes, The resistance of pure mercury at helium temperatures, Commun. Phys. Lab. Univ. Leiden **120b** (1911), reprinted in Proc. K. Ned. Akad. Wet. **13**, 1274 (1911).

[2] I. I. Mazin, Extraordinarily conventional, Nature (London) **525**, 40 (2015).

[3] J. A. Flores-Livas, L. Boeri, A. Sanna, G. Profeta, R. Arita, and M. Eremets, A perspective on conventional high-temperature superconductors at high pressure: Methods and materials, Phys. Rep. **856**, 1 (2020).

[4] J. Nagamatsu, N. Nakagawa, T. Muranaka, Y. Zenitani, and J. Akimitsu, Superconductivity at 39 K in magnesium diboride, Nature (London) **410**, 63 (2001).

[5] H. Rosner, W. E. Pickett, S. L. Drechsler, A. Handstein, G. Behr, G. Fuchs, K. Nenkov, K. H. Muller, and H. Eschrig, Electronic structure and weak electron-phonon coupling in TaB_2, Phys. Rev. B **64**, 144516 (2001).

[6] J. S. Slusky, N. Rogado, K. A. Regan, M. A. Hayward, P. Khalifah, T. He, K. Inumaru, S. M. Loureiro, M. K. Haas,

H. W. Zandbergen, and R. J. Cava, Loss of superconductivity with the addition of Al to MgB_2 and a structural transition in $Mg_{1-x}Al_xB_2$, Nature (London) **410**, 343 (2001).

[7] N. I. Medvedeva, A. L. Ivanovskii, J. E. Medvedeva, and A. J. Freeman, Electronic structure of superconducting MgB_2 and related binary and ternary borides, Phys. Rev. B **64**, 020502(R) (2001).

[8] N. Barbero, T. Shiroka, B. Delley, T. Grant, A. J. S. Machado, Z. Fisk, H. R. Ott, and J. Mesot, Doping-induced superconductivity of ZrB_2 and HfB_2, Phys. Rev. B **95**, 094505 (2017).

[9] T. Bazhirov, Y. Sakai, S. Saito, and M. L. Cohen, Electron-phonon coupling and superconductivity in Li-intercalated layered borocarbide compounds, Phys. Rev. B **89**, 045136 (2014).

[10] Y. Quan and W. E. Pickett, $Li_{2x}BC_3$: Prediction of a second MgB_2-class high-temperature superconductor, Phys. Rev. B **102**, 144504 (2020).

[11] A. Schilling, M. Cantoni, J. D. Guo, and H. R. Ott, Superconductivity above 130 K in the Hg-Ba-Ca-Cu-O system, Nature (London) **363**, 56 (1993).

[12] J. F. Ge, Z. L. Liu, C. Liu, C. L. Gao, D. Qian, Q. K. Xue, Y. Liu, and J. F. Jia, Superconductivity above 100 K in single-layer FeSe films on doped $SrTiO_3$, Nature Mater. **14**, 285 (2015).

[13] B. Keimer, S. A. Kivelson, M. R. Norman, S. Uchida, and J. Zaanen, From quantum matter to high-temperature superconductivity in copper oxides, Nature (London) **518**, 179 (2015).

[14] D. C. Johnston, The puzzle of high temperature superconductivity in layered iron pnictides and chalcogenides, Adv. Phys. **59**, 803 (2010).

[15] L. Zhang, Y. Wang, J. Lv, and Y. Ma, Materials discovery at high pressures, Nature Rev. Mater. **2**, 17005 (2017).

[16] M. Miao, Y. Sun, E. Zurek, and H. Lin, Chemistry under high pressure, Nature Rev. Chem. **4**, 508 (2020).

[17] L. Gao, Y. Y. Xue, F. Chen, Q. Xiong, R. L. Meng, D. Ramirez, and C. W. Chu, Superconductivity up to 164 K in $HgBa_2Ca_{m-l}Cu_mO_{2m+2+\delta}$ (m = l, 2, and 3) under quasihydrostatic pressures. Phys. Rev. B **50**, 4260 (1994).

[18] A. P. Drozdov, M. I. Eremets, I. A. Troyan, V. Ksenofontov, and S. I. Shylin, Conventional superconductivity at 203 kelvin at high pressures in the sulfur hydride system, Nature (London) **525**, 73 (2015).

[19] D. Duan, Y. Liu, F. Tian, D. Li, X. Huang, Z. Zhao, H. Yu, B. Liu, W. Tian, and T. Cui, Pressure-induced metallization of dense $(H_2S)_2H_2$ with high-T_c superconductivity, Sci. Rep. **4**, 6968 (2014).

[20] F. Peng, Y. Sun, C. J. Pickard, R. J. Needs, Q. Wu, and Y. Ma, Hydrogen Clathrate Structures in Rare Earth Hydrides at High Pressures: Possible Route to Room-Temperature Superconductivity, Phys. Rev. Lett. **119**, 107001 (2017).

[21] H. Liu, I. I. Naumov, R. Hoffmann, N. W. Ashcroft, and R. J. Hemley, Potential high-Tc superconducting lanthanum and yttrium hydrides at high pressure, Proc. Natl. Acad. Sci. USA **114**, 6990 (2017).

[22] M. Somayazulu, M. Ahart, A. K. Mishra, Z. M. Geballe, M. Baldini, Y. Meng, V. V. Struzhkin, and R. J. Hemley, Evidence for Superconductivity above 260 K in Lanthanum Superhydride at Megabar Pressures, Phys. Rev. Lett. **122**, 027001 (2019).

[23] A. P. Drozdov, P. P. Kong, V. S. Minkov, S. P. Besedin, M. A. Kuzovnikov, S. Mozaffari, L. Balicas, F. F. Balakirev, D. E. Graf, V. B. Prakapenka, E. Greenberg, D. A. Knyazev, M. Tkacz, and M. I. Eremets, Superconductivity at 250 K in lanthanum hydride under high pressures, Nature (London) **569**, 528 (2019).

[24] E. Snider, N. Dasenbrock-Gammon, R. McBride, M. Debessai, H. Vindana, K. Vencatasamy, K. V. Lawler, A. Salamat, and R. P. Dias, Room-temperature superconductivity in a carbonaceous sulfur hydride, Nature (London) **586**, 373 (2020).

[25] C. Pei, J. Zhang, Q. Wang, Y. Zhao, L. Gao, C. Gong, S. Tian, R. Luo, Z. Y. Lu, H. Lei, K. Liu, and Y. Qi, arXiv:2105.13250.

[26] Y. Quan, K. W. Lee, and W. E. Pickett, MoB_2 under pressure: Superconducting Mo enhanced by boron, Phys. Rev. B **104**, 224504 (2021).

[27] A. B. Migdal, Interaction between electrons and lattice vibrations in a normal metal, Sov. Phys. JETP **7**, 996 (1958).

[28] G. M. Eliashberg, Interactions between electrons and lattice vibrations in a superconductor, Sov. Phys. JETP **11**, 696 (1960).

[29] H. J. Choi, D. Roundy, H. Sun, M. L. Cohen, and S. G. Louie, The origin of the anomalous superconducting properties of MgB_2, Nature **418**, 758 (2002).

[30] G. Kresse and J. J. Hafner, Ab initio molecular dynamics for open-shell transition metals, Phys. Rev. B **48**, 13115 (1993).

[31] G. Kresse and J. Furthmüller, Efficiency of ab-initio total energy calculations for metals and semiconductors using a plane-wave basis set, Comput. Mater. Sci. **6**, 15 (1996).

[32] P. E. Blöchl, Projector augmented-wave method, Phys. Rev. B **50**, 17953 (1994).

[33] J. P. Perdew, K. Burke, and M. Ernzerhof, Generalized Gradient Approximation Made Simple, Phys. Rev. Lett. **77**, 3865 (1996).

[34] P. Giannozzi, S. Baroni, N. Bonini, M. Calandra, R. Car, C. Cavazzoni, D. Ceresoli, G. L. Chiarotti, M. Cococcioni, I. Dabo, A. Dal Corso, S. de Gironcoli, S. Fabris, G. Fratesi, R. Gebauer, U. Gerstmann, C. Gougoussis, A. Kokalj, M. Lazzeri, L. Martin-Samos, N. Marzari *et al.* QUANTUM ESPRESSO: a modular and open-source software project for quantum simulations of materials, J. Phys.: Condens. Matter **21**, 395502 (2009).

[35] M. Schlipf and F. Gygi, Optimization algorithm for the generation of ONCV pseudopotentials, Comput. Phys. Commun. **196**, 36 (2015).

[36] K. H. Lee, K. J. Chang, and M. L. Cohen, First-principles calculations of the Coulomb pseudopotential μ^*: Application to Al, Phys. Rev. B **52**, 1425 (1995).

[37] P. Giannozzi, O. Andreussi, T. Brumme, O. Bunau, M. Buongiorno Nardelli, M. Calandra, R. Car, C. Cavazzoni, D. Ceresoli, M. Cococcion, N. Colonna, I. Carnimeo, A. Dal Corso, S. de Gironcoli, P. Delugas, R. A. DiStasio Jr., A. Ferretti, A. Floris, G. Fratesi, G. Fugallo, R. Gebauer, U. Gerstmann, F. Giustino *et al.* Advanced capabilities for materials modelling with Quantum ESPRESSO, J. Phys.: Condens. Matter **29**, 465901 (2017).

[38] E. Sanville, S. D. Kenny, R. Smith, and G. Henkelman, Improved grid-based algorithm for Bader charge allocation, J. Comput. Chem. **28**, 899 (2007).

[39] See Supplemental Material at http://link.aps.org/supplemental/10.1103/PhysRevB.106.064507 for the calculated band structures and Fermi sheets of α-MoB_2, phonon spectrums of MgB_2 and compressed α-MoB_2, electronic density of states of Re-doped α-MoB_2, and electronic structure of β-MoB_2.

[40] E. Kaxiras, *Atomic and Electronic Structure of Solids* (Cambridge University Press, New York, 2003).

[41] L. Liu, C. Wang, S. Yi, K. W. Kim, J. Kim, and J. H. Cho, Microscopic mechanism of room-temperature superconductivity in compressed LaH_{10}, Phys. Rev. B **99**, 140501(R) (2019).

[42] Y. Quan and W. E. Pickett, Van Hove singularities and spectral smearing in high-temperature superconducting H_3S, Phys. Rev. B **93**, 104526 (2016).

[43] S. Baroni, S. de Gironcoli, A. Dal Corso, and P. Giannozzi, Phonons and related crystal properties from density-functional perturbation theory, Rev. Mod. Phys. **73**, 515 (2001).

[44] F. S. Khan and P. B. Allen, Deformation potentials and electron-phonon scattering: Two new theorems, Phys. Rev. B **29**, 3341 (1984).

[45] W. L. McMillan, Transition temperature of strong-coupled superconductors, Phys. Rev. **167**, 331 (1968).

[46] X. Zhang, M. Zhao, and F. Liu, Enhancing superconductivity in bulk β-Bi_2Pd by negative pressure induced by quantum electronic stress, Phys. Rev. B **100**, 104527 (2019).

[47] E. R. Margine and F. Giustino, Anisotropic migdal-eliashberg theory using wannier functions, Phys. Rev. B **87**, 024505 (2013).

[48] X. K. Chen, M. J. Konstantinović, J. C. Irwin, D. D. Lawrie, and J. P. Franck, Evidence for Two Superconducting Gaps in MgB_2, Phys. Rev. Lett. **87**, 157002 (2001).